

Inversion/Mirror Symmetry-Protected Dirac Cones in Distorted Ruby Lattices

Lei Sun(孙雷)¹, Xiaoming Zhang(张晓明)¹, Han Gao(高涵)¹, Jian Liu(刘剑)¹,
Feng Liu(刘锋)², and Mingwen Zhao(赵明文)^{1,3*}

¹*School of Physics and State Key Laboratory of Crystal Materials,
Shandong University, Jinan 250100, China*

²*Department of Materials Science and Engineering, University of Utah, Salt Lake City, Utah 84112, USA*

³*Collaborative Innovation Center of Light Manipulations and Applications, Shandong Normal University,
Jinan 250358, China*

(Received 17 September 2020; accepted 4 November 2020; published online 8 December 2020)

The exotic electronic band structures of Ruby and Star lattices, characterized by Dirac cone and nontrivial topology, offer a unique platform for the study of two-dimensional (2D) Dirac materials. In general, an ideal isotropic Dirac cone is protected by time reversal symmetry and inversion, so that its robustness against lattice distortion is not only of fundamental interest but also crucial to practical applications. Here we systematically investigate the robustness of Dirac cone in a Ruby lattice against four typical lattice distortions that break the inversion and/or mirror symmetry in the transition from Ruby to Star. Using a tight-binding approach, we show that the isotropic Dirac cones and their related topological features remain intact in the rotationally distorted lattices that preserve the inversion symmetry (*i*-Ruby lattice) or the in-plane mirror symmetry (*m*-Ruby lattice). On the other hand, the Dirac cones are gapped in the *a*- and *b*-Ruby lattices that break both these lattice symmetries or inversion. Furthermore, a rotational unitary matrix is identified to transform the original into the distorted lattice. The symmetry-protected Dirac cones were also verified in photonic crystal systems. The robust Dirac cones revealed in the non-mirror symmetric *i*-Ruby and non-centrosymmetric *m*-Ruby lattices provide a general guidance for the design of 2D Dirac materials.

PACS: 71.20.-b, 73.20.At, 73.22.Gk, 42.70.Qs

DOI: 10.1088/0256-307X/37/12/127102

Motivated by the intriguing properties and extensive applications of graphene,^[1–3] two-dimensional (2D) Dirac materials have been drawing increasing interests in physics and materials science. The electronic band structures of Dirac materials can be featured by the linear energy-momentum dispersion (named as Dirac cone) near the Fermi level which differs significantly to the parabolic dispersion relation in normal semiconductors. The carriers near the Fermi level behavior as the massless Dirac fermions that obey the Dirac equation. Such a linear energy-momentum dispersion was also correlated to a number of fascinating properties, such as quantum anomalous hall effect (QAHE),^[4–8] quantum spin hall effect (QSHE)^[9–11] and even fractional quantum hall effect (FQHE),^[12–18] bringing about new concepts for the next-generation electronic devices.

The relation between lattice symmetry and electronic structure provides a powerful mean for the exploration of 2D Dirac materials. In general, an ideal isotropic Dirac cone is protected by time reversal symmetry and inversion. According to this principle, a number of lattice models, such as honeycomb,^[1–3] Kagome,^[19–22] Ruby,^[23–25] and Star lattices,^[26–28] have been proposed to possess intrinsic Dirac cones in their electronic band structures, accompanied by topologically nontrivial electronic states. The Dirac

cones originating from the energy band crossing can be described by a simple Hamiltonian of a two-band system as follows:

$$H(\mathbf{k}) = \begin{bmatrix} H_{11}(\mathbf{k}) - E & H_{12}(\mathbf{k}) \\ H_{21}(\mathbf{k}) & H_{22}(\mathbf{k}) - E \end{bmatrix}. \quad (1)$$

The appearance of Dirac cones corresponds to the degenerate solutions of this Hamiltonian, i.e., the determinant of $H(\mathbf{k})$ should be zero and the following equations should be fulfilled: $H_{11}(\mathbf{k}) = H_{22}(\mathbf{k})$, $H_{12}(\mathbf{k}) = 0$, and $H_{21}(\mathbf{k}) = 0$ at the Dirac points. Intrinsically, these equations should be simultaneously satisfied to have a degeneracy, known as the von Neumann–Wigner theorem.^[29,30] However, the number of variables (k_x, k_y) is usually less than the number of the equations to determine the Dirac points, making 2D Dirac materials rare. Spatial inversion symmetry can lead to $H_{11}(\mathbf{k}) = H_{22}(\mathbf{k})$ and thus is regarded as one of the requirements of 2D Dirac materials. Additionally, mirror symmetry is also included in these lattice models, but the necessity has never been demonstrated.

Among these lattice models, the Ruby and Star lattices are of particular interest, owing to the flexibility in electronic structures and abundant physical phenomena.^[12–18] The Ruby lattice is constructed by placing regular triangles at the vertexes of a honey-

Supported by the National Natural Science Foundation of China (Grant No. 11774201), and the Taishan Scholarship of Shandong Province.

*Corresponding author. Email: zmw@sdu.edu.cn

© 2020 Chinese Physical Society and IOP Publishing Ltd

comb lattice in an “edge-to-edge” way, as shown in Fig. 1(a), while the “vertex-to-vertex” arrangement of triangles leads to the Star lattice, as shown in Fig. 1(f). Both spatial inversion symmetry and mirror symmetry are involved in these two lattices with the point group of D_{6h} . The Dirac cones and topologically nontrivial states inherited in these two lattices have been demonstrated from different approaches.^[23–28] The topological flat bands originating from the ge-

ometric frustration of Bloch wave functions in these lattices pave a new way for achieving fractional quantum Hall effects.^[12–18] The highly-localized electron density of states at the Fermi level may also lead to strong electron correlation interaction and superconducting properties. A 2D graphene-like carbon nitride has also been proposed as a candidate material to realize the Dirac cones and nontrivial topology of the Ruby lattice.^[31]

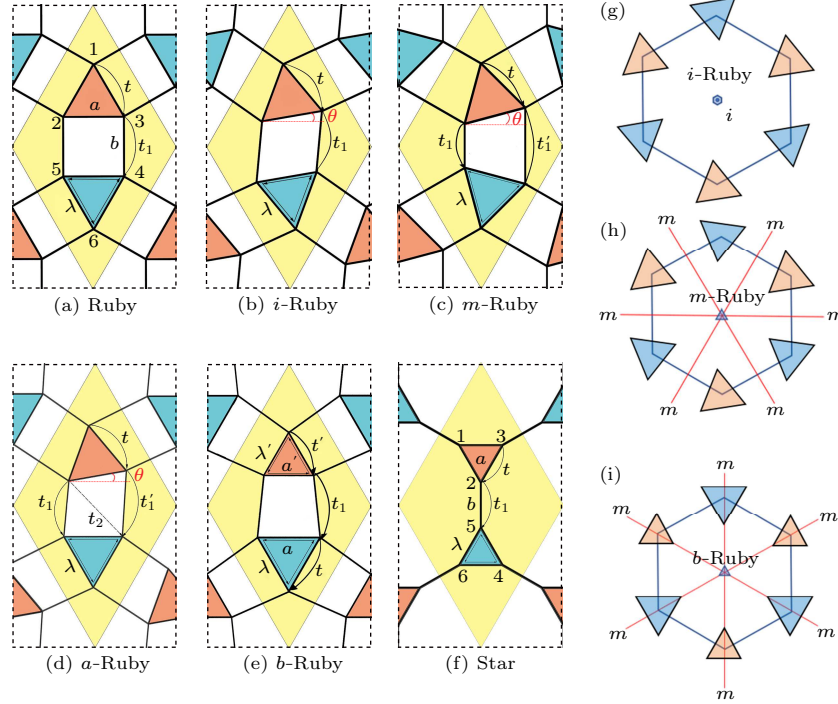


Fig. 1. Schematic of (a) perfect Ruby, (b) *i*-Ruby, (c) *m*-Ruby, (d) *a*-Ruby, (e) *b*-Ruby, and (f) Star lattices. Here ab are set to be the bond lengths of the Ruby lattice; $t(t')$, $t_1(t'_1)$ and t_2 represent different hopping amplitudes, respectively; $\lambda(\lambda')$ represents the strength of SOC indicated by the triangular arrows in the figure. The yellow rhombus indicates the shape of the unitcell. Schematic representations of the structural symmetries of (g) *i*-Ruby, (h) *m*-Ruby and (i) *b*-Ruby lattices. The hexagons indicate the arrangement of the triangle centers.

It is interesting to see the gap between the geometries of Ruby and Star lattices. In addition to the highly symmetric edge-to-edge and vertex-to-vertex patterns, there are obvious abundant lattice structures with arbitrary orientation between the two adjacent triangles. Additionally, structural distortion which is inevitable in the material realization of the Ruby and Star models may break the structural symmetries and affect the electronic band structures and topological properties. However, the relevant theoretical investigations on the distorted lattices have rarely been reported.

Here, we bridge the “gap” by four typical distorted Ruby lattices, named as *i*-Ruby, *m*-Ruby, *a*-Ruby and *b*-Ruby, as shown in Figs. 1(b)–1(e), and reveal the symmetry-dependent electronic band structures using a tight-binding (TB) method. The spatial reversion or/and mirror symmetry of the lattices are broken by rotating or scaling the two adjacent triangles in different ways. We demonstrate that the isotropic Dirac

cones and their related topological features remain intact in the *i*-Ruby and *m*-Ruby lattices that preserve the inversion symmetry or the in-plane mirror symmetry, as shown in Figs. 1(g) and 1(h). On the other hand, the Dirac cones are gapped in the *a*- and *b*-Ruby lattices that break both these lattice symmetries or inversion. Furthermore, a rotational unitary matrix is identified to transform the distorted lattices into the Ruby or Star lattice. The symmetry-protected Dirac cones in these lattices were also verified in photonic crystal systems. The robust Dirac cones protected by the mirror symmetry found in the non-centrosymmetric *m*-Ruby lattice extends the scope the 2D materials, offering a general principle for the design of 2D Dirac materials.

The four typical distortions of the Ruby lattice considered in this work were constructed by rotating or scaling the two triangles in the unit cell in different ways, while the centers of these triangles were fixed to a perfect honeycomb arrangement. The synchronous

rotation (clockwise or anticlockwise) of the two triangles lifts the in-plane mirror symmetry but retains the spatial inversion symmetry, as shown in Figs. 1(b) and 1(g), reducing the point symmetry from D_{6h} to C_{6h} , which is referred to as *i*-Ruby lattice. When the two triangles are rotated one clockwise another anticlockwise, the spatial inversion symmetry is broken, but the symmetry plane vertical to the line between the centers of the two triangles is preserved, as shown in Figs. 1(c) and 1(h). The point group is reduced to D_{3h} . The resulted lattice is named as *m*-Ruby lattice. Both *i*-Ruby lattice and *m*-Ruby lattices convert to the Star lattice at $\theta = 60^\circ$. As the two triangles

are rotated asynchronously, e.g., rotating only one triangle, both inversion and in-plane mirror symmetries of the lattice are lifted, as shown in Fig. 1(d), which is named as *a*-Ruby lattice. The point group is further reduced to C_{3h} . For the *b*-Ruby lattice, the two triangles are respectively scaled up and back, liking “breathing”, which lifts the spatial inversion, but preserves the in-plane mirror symmetries parallel to the line between the centers of the two triangles, as shown in Fig. 1(i). The *b*-Ruby lattice has the same point group (D_{3h}) as the *m*-Ruby lattice, but different locations of the mirror planes.

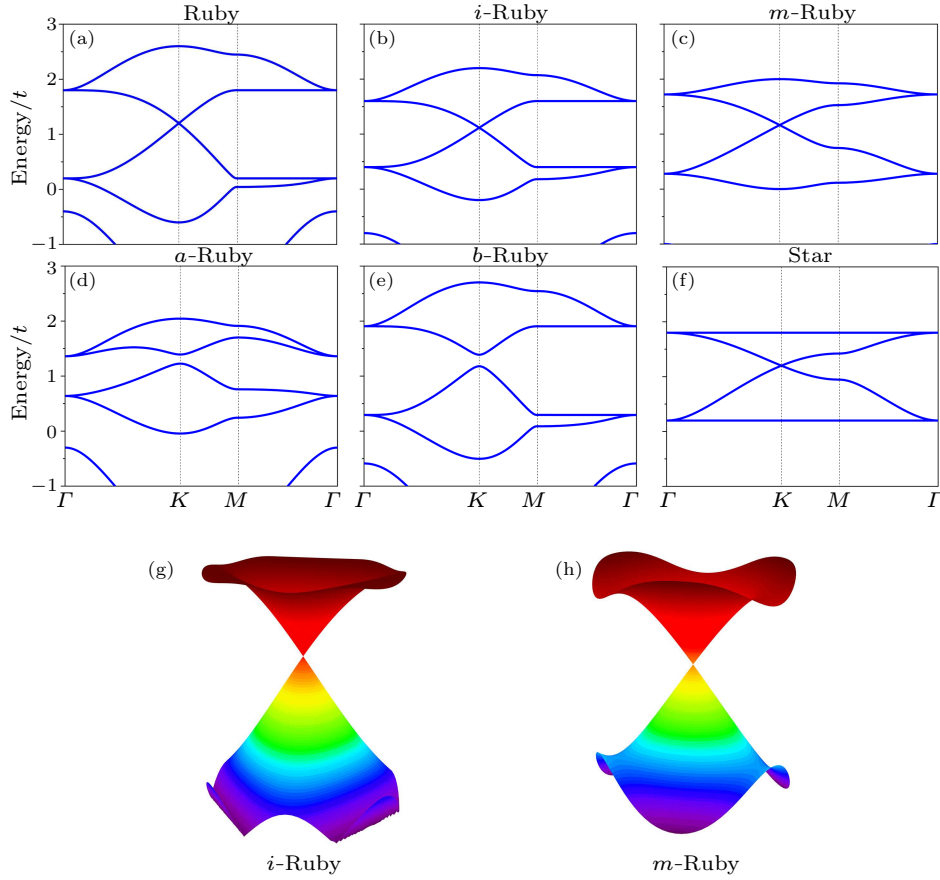


Fig. 2. Schematic of the energy band of Ruby lattice without SOC. (a) Perfect Ruby with $t_1 = 0.8t$; (b) *i*-Ruby lattice $t_1 = 0.6t$; (c) *m*-Ruby lattice with $t_1 = 0.8t$, $t'_1 = 0.2t$; (d) *a*-Ruby lattice with $t_1 = 0.8t$, $t'_1 = 0.4t$, $t_2 = 0.5t$; (e) *b*-Ruby lattice with $t_1 = 0.8t$, $t' = 1.2t$ and (f) Star lattice $t_1 = 0.8t$. The Dirac cones in (g) *i*-Ruby and (h) *m*-Ruby lattices

We build a spin-free tight-binding (TB) Hamiltonian of the distorted Ruby lattices as follows:

$$H_0 = - \sum_{\langle i,j \rangle} t_{ij} c_i^\dagger c_j + \text{H.c.}, \quad (2)$$

where c_i^\dagger and c_i are the creation and annihilation operators of the i th site, respectively. For simplification, only the hopping between adjacent sites with the amplitude of t_{ij} were involved, as indicated in Fig. 1, and the on-site energy is set to zero (see the Supporting Information for details).

For the *i*-Ruby lattice, there are two types of nearest-neighbor hopping terms, intra-triangular hopping (t) and inter-triangular hopping (t_1), as shown in Fig. 1(b). The base vectors of the distorted Ruby lattices are fixed during the rotation. The *i*-Ruby lattice converges to the perfect Ruby lattice at $\theta = 0$. The energy spectra of the perfect Ruby and the *i*-Ruby lattices obtained from the TB Hamiltonian are plotted in Figs. 2(a) and 2(b). Obviously, the isotropic Dirac cones at the K and K' points of the undistorted Ruby lattice are well preserved in the *i*-Ruby lattice, as shown in Fig. 2(g). More interestingly, if the hop-

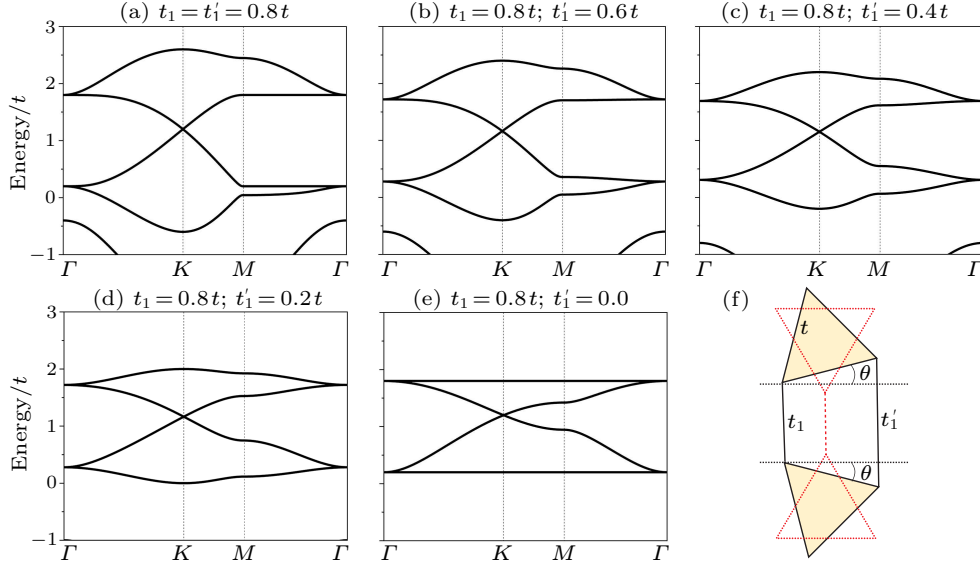


Fig. 3. (a)–(e) The energy bands of *m*-Ruby lattice with different $t_1'/t = 0.8, 0.6, 0.4, 0.2, 0$. (f) Schematic representation of lattice and hopping parameters of *m*-Ruby lattice.

For the *b*-Ruby lattice, the inversion symmetry is lifted due to the different size of triangles (a and a'). Two types of intra-triangular hopping (t' and t) and one type of inter-triangular hopping (t_1) are considered in the TB Hamiltonian, as shown in Fig. 1(e). The *b*-Ruby lattice bears the same point group (D_{3h}) as the *m*-Ruby lattice but different locations of mirror planes, as shown in Figs. 1(h) and 1(i). Such a difference leads to a different electronic band structure. The Dirac cones are gaped in the *b*-Ruby lattice, as shown in Fig. 2(e), indicating that the mirror symmetry in the *b*-Ruby is incapable of preserving the Dirac cones. Notably, the mirror symmetry is identical to that of the graphene-like boron nitride lattice (g-BN). Compared to graphene, the spatial inversion symmetry is removed in the g-BN lattice, opening a band gap at the Dirac points. In this sense, the *b*-Ruby lattice can be regarded as an analog of the g-BN lattice. The band gap in the *b*-Ruby lattice offers a promising strategy of regulating the electronic band structure of Ruby lattice to fulfill the requirement of electronic devices where a band gap is needed.

To investigate the topological properties of these lattices, an intrinsic SOC term is introduced in the Hamiltonian

$$H = H_0 + i \sum_{\langle ij \rangle} \lambda_{ij} v_{ij} c_i^\dagger \sigma_z c_j + \text{H.c.}, \quad (5)$$

where λ_{ij} represents the strength of SOC, $v_{ij} = d_{ij}^1 \times d_{ij}^2 = \pm 1$, d_{ij}^1 and d_{ij}^2 are the nearest neighbor lattice vectors connecting sites i and j . For simplification, we only consider the SOC between same spin states within the triangles, as shown in Fig. 1. In fact, the simplified SOC item does not give crucial influence on the topology of the model, as shown in Fig. S1 in the Supporting Information. Similar to the case of undistorted Ruby lattice, the Dirac cones of the *i*-Ruby and

m-Ruby lattices are gaped by SOC effect. The energy degeneracy at the Γ point was also lifted. The topological properties of these lattices can be verified from the non-zero topological invariants. Here, we calculate the Chern number (also known as the TKNN number) of the lattice using the Kubo formula:^[33]

$$C = \frac{1}{2\pi} \int_{\text{BZ}} \sum_n f_n \Omega_n(k) d^2k, \quad (6)$$

with

$$\Omega_n(k) = - \sum_{n' \neq n} 2\text{Im} \frac{\langle \Psi_{nk} | \hat{v}_x | \Psi_{n'k} \rangle \langle \Psi_{n'k} | \hat{v}_y | \Psi_{nk} \rangle}{(\varepsilon_{n'k} - \varepsilon_{nk})},$$

where Ψ_{nk} and ε_{nk} are the eigenstate and eigenvalue of the band n , respectively; f_n is the Fermi distribution function, and \hat{v} is the velocity operator. The total Chern numbers of the bands below the Dirac point are labeled in Fig. 4. Clearly, both *i*-Ruby and *m*-Ruby lattices have the Chern number of -1 , indicating that the gaps opened at the Dirac point due to SOC are topologically nontrivial. This is quite similar to the cases of honeycomb lattice^[1–3] and Kagome lattice,^[19–22] where SOC opens a topologically nontrivial band gap at the Dirac point. For *a*-Ruby and *b*-Ruby lattices, however, the band gap opened up at the Dirac point due to the absence of spatial inversion symmetry is topologically trivial under a weak SOC strength, similar to the case of BN honeycomb lattice.

The topological properties of the lattices can also be verified from the edge states of the nanoribbons with half-infinite width. We have calculated the electronic band structures of these nanoribbons according to the TB Hamiltonians, as plotted in Fig. 5. For the *i*-Ruby and *m*-Ruby lattices, two edge bands within the band gap connect the top and bottom bulk bands and intersect at the Γ point, in agreement with the

Chern number $C = -1$, which is similar to the case of perfect Ruby lattice. For the a -Ruby and b -Ruby lattices, however, the edge bands have no intersection

within the band gap, implying that the band gap is topologically trivial, in consistency with the zero Chern number.

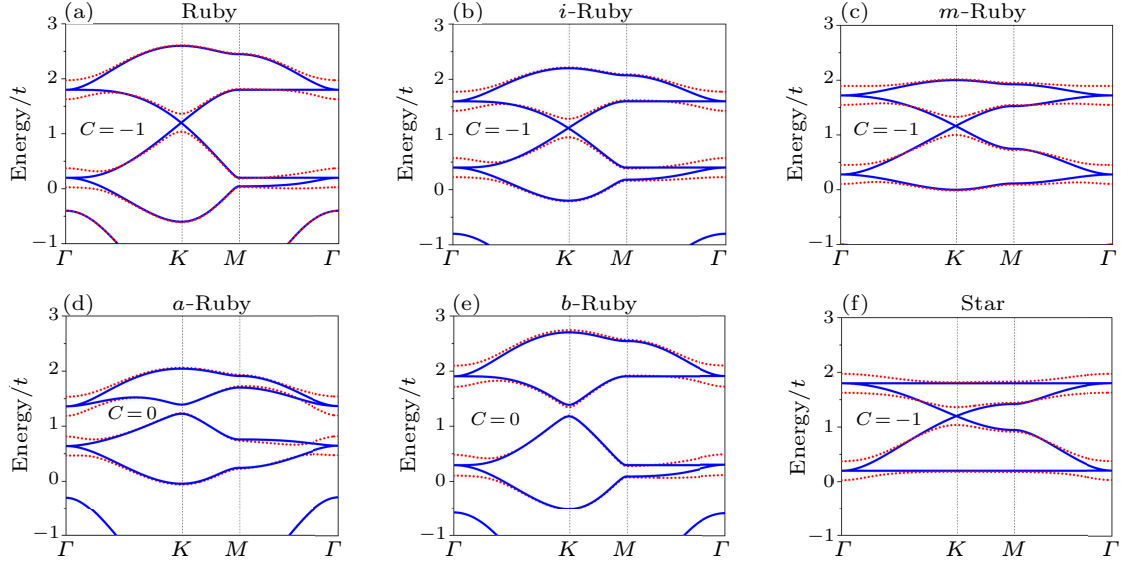


Fig. 4. The TB electronic band structures of (a) Ruby, (b) i -Ruby, (c) m -Ruby, (d) a -Ruby, (e) b -Ruby, and Star lattices (f). The blue solid lines and red dotted lines represent the bands without and with SOC. The SOC strength is set to $\lambda = 0.1t$ (this value would be smaller in a, b -Ruby). The hopping parameters are the same as those of Fig. 2. The Chern number C of the bands below the Dirac points is also presented in the figure.

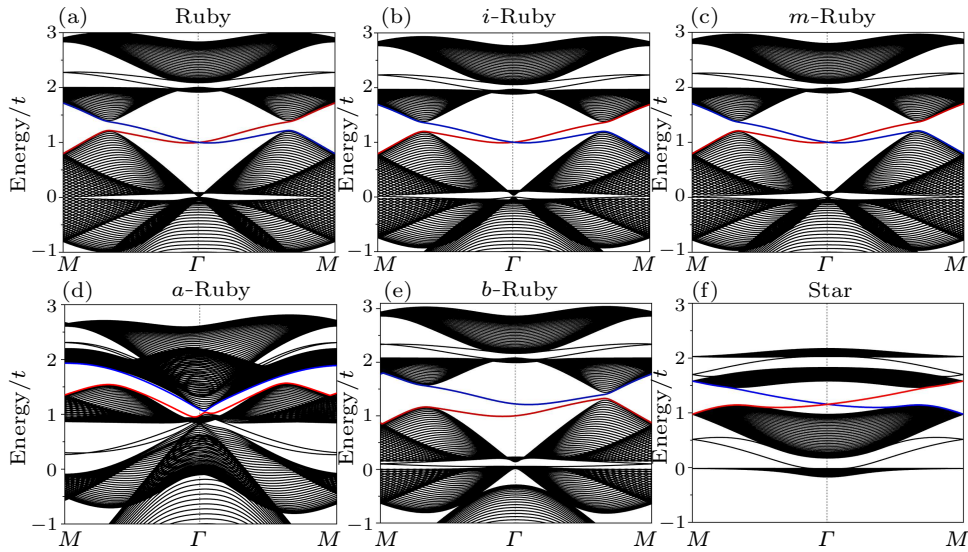


Fig. 5. The electronic band structures of the nanoribbons of (a) perfect Ruby, (b) i -Ruby, (c) m -Ruby, (d) a -Ruby, (e) b -Ruby, and (e) Star lattices. The width of the nanoribbon is 20. The red and blue lines represent the edge states on different sides.

From the above analysis, we can see the two pathways connecting Ruby lattice to Star lattice, while preserving the Dirac cones and topologically nontrivial features. One is rotating the two triangles synchronously (i -Ruby model) with an angle θ from 0° to 60° . The mirror symmetry is broken, but the inversion symmetry is retained in this pathway. The other is rotating the two triangles asynchronously (m -

Ruby model), one clockwise (from 0° to 60°) the other anticlockwise (from 0° to -60°), in which the mirror symmetry is preserved, but the inversion symmetry is broken. The robust Dirac cones and topological nontriviality along with the structural transition between Ruby and Star models offer promising strategies to achieve exotic scenarios, such as QAHE, QSHE or FQHE.

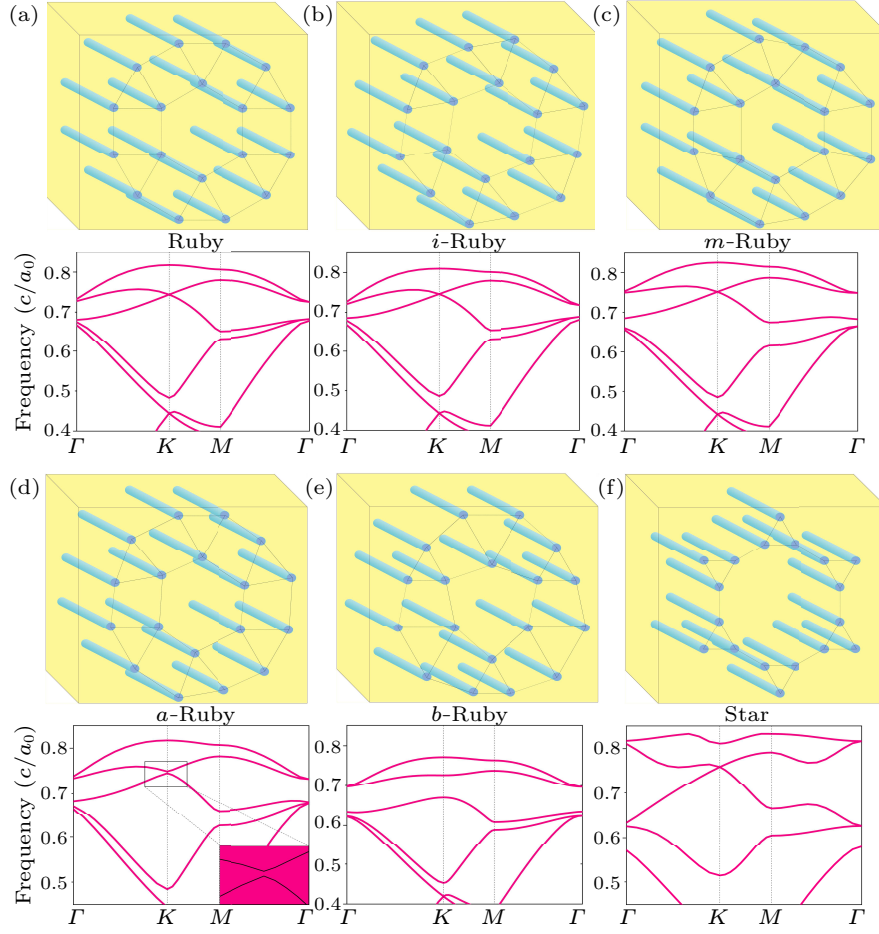


Fig. 6. The numerical simulated frequency spectra of the photonic waveguides of (a) Ruby, (b) *i*-Ruby, (c) *m*-Ruby, (d) *a*-Ruby, (e) *b*-Ruby, and (f) Star lattices. The schematic diagram of arrays of photonic waveguides on a vacuum substrate are also drawn.

Finally, we adopt photonic waveguide systems to demonstrate the interesting scenarios of the above-mentioned electronic band structures. In a 2D photonic lattice, the diffraction behavior of a photon can be expressed by the following equation analogous to the Schrödinger equation of electrons:

$$-\frac{1}{\sqrt{\varepsilon(\mathbf{r})}} \nabla^2 \frac{1}{\sqrt{\varepsilon(\mathbf{r})}} F_z(\mathbf{r}) = \frac{\omega^2}{c^2} F_z(\mathbf{r}), \quad (7)$$

where $\varepsilon(\mathbf{r})$ is the dielectric constant which is highly dependent on the patterns of the waveguide arrays, $F_z(\mathbf{r}) = \sqrt{\varepsilon(\mathbf{r})} E_z(\mathbf{r})$, ω and c are the frequency and speed of light in vacuum. According to Bloch's theorem, $F_z(\mathbf{r})$ can be expanded by the normalized orthogonal field $\psi_i(\mathbf{r})$, which is assumed to localize at the site i ,

$$F_z(\mathbf{r}) = \sum_{\mathbf{R}} e^{i\mathbf{k}\cdot\mathbf{R}} \sum_{i=1}^6 c_i \psi_i(\mathbf{r} - \mathbf{R}), \quad (8)$$

where c_i is the coefficient of $\psi_i(\mathbf{r})$. Equation (7) can be reduced to a linear homogeneous equation set of c_i , in analogy to the TB strategy. Therefore, as the waveguide arrays are aligned in the pattern similar to

the lattice models, the photonic band structures $\omega(\mathbf{k})$ will reflect the properties of the TB band structures of the lattices. According to the plane-wave method,^[34] we can convert Eq. (7) to the reciprocal space as follows:

$$\sum_{\mathbf{G}'} \varepsilon^{-1}(\mathbf{G} - \mathbf{G}') |\mathbf{k} + \mathbf{G}'|^2 E(\mathbf{G}') = \frac{\omega^2}{c^2} E(\mathbf{G}) \quad (9)$$

to get the photonic band structures $\omega(\mathbf{k})$, where \mathbf{G} represents reciprocal vectors, $\varepsilon(\mathbf{G})$ and $E(\mathbf{G})$ are the Fourier transforms of $\varepsilon(\mathbf{r})$ and $E(\mathbf{r})$, respectively. Here, we arrange the waveguide arrays according to the lattice models described above. The distance between the two adjacent waveguides is $11 \mu\text{m}$, and the radius of each waveguide is $2 \mu\text{m}$. The waveguide and substrate are, respectively, set to silicon and vacuum. Each waveguide retains only one mode. Experimentally, these photonic waveguide systems can be achieved by the femtosecond direct writing method.^[35]

The photonic band structures of the six photonic waveguide systems constructed according to perfect Ruby, *i*-Ruby, *m*-Ruby, *a*-Ruby, *b*-Ruby and Star lattice models are plotted in Fig. 6. We can see the Dirac cones of the perfect Ruby, *i*-Ruby, *m*-Ruby and Star

lattices and the band gaps opened at the Dirac points of *a*-Ruby and *b*-Ruby lattices. The photonic waveguide systems are rather complicated compared with the TB models of these lattices. However, the Dirac cones and the band gaps of the photonic band structure are consistent with the results of the TB models, confirming the robust Dirac cones of these distorted Ruby lattices. These results also provide a useful guidance for the design of photonic waveguide systems with desired photonic properties.

In summary, we have proposed four types of distorted Ruby lattices with different symmetries to bridge the gap between Ruby lattice and Star lattice. On the basis of tight-binding Hamiltonians, we demonstrate that the Dirac cones and the associated topological properties of the perfect Ruby and Star lattices can be well preserved in *i*-Ruby and *m*-Ruby lattices, which are protected by spatial inversion symmetry and mirror symmetries, respectively. The Dirac cones found in the non-centrosymmetric *m*-Ruby broaden the scope of the 2D Dirac materials. Band gap appears at the Dirac points in the *a*-Ruby lattice where both inversion and mirror symmetries are lifted. The *b*-Ruby lattice can be regarded as an analog of the BN honeycomb lattice, in which the absence of spatial inversion symmetry opens band gaps at the Dirac points. The lattice-symmetry-dependent electronic band structures are also verified in photonic waveguide systems. The robust Dirac cones in *i*-Ruby and *m*-Ruby lattices and the tunable band gaps of the *a*-Ruby and *b*-Ruby lattices offer promising models for 2D topological insulators and valleytronics materials

References

- [1] Novoselov K S, Geim A K, Morozov S V, Jiang D, Zhang Y, Dubonos S V, Grigorieva I V and Firsov A A 2004 *Science* **306** 666
- [2] Yao Y, Ye F, Qi X L, Zhang S C and Fang Z 2007 *Phys. Rev. B* **75** 041401
- [3] Wang A Z, Zhao X R, Zhao M W, Zhang X M, Feng Y P and Liu F 2018 *J. Phys. Chem. Lett.* **9** 614
- [4] Hu J, Zhu Z and Wu R 2015 *Nano Lett.* **15** 2074
- [5] Qiao Z, Ren W, Chen H, Bellaiche L, Zhang Z, MacDonald A H and Niu Q 2014 *Phys. Rev. Lett.* **112** 116404
- [6] Haldane F D 1988 *Phys. Rev. Lett.* **61** 2015
- [7] Liu J, Meng S and Sun J T 2019 *Nano Lett.* **19** 3321
- [8] Liu H, Sun J T, Liu M and Meng S 2018 *J. Phys. Chem. Lett.* **9** 6709
- [9] Kane C L and Mele E J 2005 *Phys. Rev. Lett.* **95** 226801
- [10] Bernevig B A and Zhang S C 2006 *Phys. Rev. Lett.* **96** 106802
- [11] Kane C L and Mele E J 2005 *Phys. Rev. Lett.* **95** 146802
- [12] Sun K, Gu Z C, Katsura H and Sarma S D 2011 *Phys. Rev. Lett.* **106** 236803
- [13] Neupert T, Santos L, Chamon C and Mudry C 2011 *Phys. Rev. Lett.* **106** 236804
- [14] Jain J K and Jeon S 2005 *Phys. Rev. B* **72** 201303
- [15] Du X, Skachko I, Duerr F, Luican A and Andrei E Y 2009 *Nature* **462** 192
- [16] Read N and Green D 2000 *Phys. Rev. B* **61** 10267
- [17] Tang E, Mei J W and Wen X G 2011 *Phys. Rev. Lett.* **106** 236802
- [18] Bolotin K I, Ghahari F, Shulman M D, Stormer H L and Kim P 2009 *Nature* **462** 196
- [19] Zhang S *et al.* 2019 *Phys. Rev. B* **99** 100404(R)
- [20] Jiang W, Kang M, Huang H, Xu H, Low T and Liu F 2019 *Phys. Rev. B* **99** 125131
- [21] Guo H M and Franz M 2009 *Phys. Rev. B* **80** 113102
- [22] Liu X Y and Yan W G 2013 *Physica A* **392** 5615
- [23] Hu X, Kargarian M and Fiete G A 2011 *Phys. Rev. B* **84** 155116
- [24] Lin K Y and Ma W J 1983 *J. Phys. A* **16** 3895
- [25] Lin K Y 1984 *J. Phys. A* **17** 3201
- [26] Chen M and Wan S 2012 *J. Phys.: Condens. Matter* **24** 325502
- [27] Owerre S A 2017 *J. Phys.: Condens. Matter* **29** 185801
- [28] Chen W C, Liu R, Wang Y F and Gong C D 2012 *Phys. Rev. B* **86** 085311
- [29] Neumann J V, Wigner W 1929 *Z. Phys.* **30** 467
- [30] Lifshitz E M and Landau L D 1981 *Quantum Mechanics (Non-Relativistic Theory)* 3rd edn (Oxford: Reed Educational and Professional Publishing Ltd)
- [31] Wang A, Zhang X and Zhao M 2014 *Nanoscale* **6** 11157
- [32] Yang B, Zhang X M, Wang A Z and Zhao M W 2019 *J. Phys.: Condens. Matter* **31** 155001
- [33] Yao Y, Kleinman L, MacDonald A H, Sinova J, Jungwirth T, Wang D S, Wang E and Niu Q 2004 *Phys. Rev. Lett.* **92** 037204
- [34] Takeda H, Takashima T and Yoshino K 2004 *J. Phys.: Condens. Matter* **16** 6317
- [35] Szameit A and Nolte S 2010 *J. Phys. B* **43** 163001

Supporting Information: Inversion/mirror symmetry-protected Dirac cones in distorted Ruby lattices

Lei Sun (孙雷),¹ Xiaoming Zhang(张晓明),¹ Han Gao(高涵),¹ Jian Liu(刘剑),¹ Feng Liu(刘锋),² and Mingwen Zhao(赵明文),^{1,3*}

¹*School of Physics and State Key Laboratory of Crystal Materials, Shandong University, Jinan, Shandong, 250100, China*

²*Department of Materials Science and Engineering, University of Utah, Salt Lake City, Utah 84112, USA*

³*Collaborative Innovation Center of Light Manipulations and Applications, Shandong Normal University, Jinan 250358, China*

*Corresponding Author: zmw@sdu.edu.cn

SI. Tight-Binding Hamiltonians

i-Ruby lattice

$$H_0^{iR}(\mathbf{k}) = -t \begin{pmatrix} 0 & e^{i\varphi_{12}} & e^{i\varphi_{13}} & \gamma e^{i\varphi_{14}} & \gamma e^{i\varphi_{15}} & 0 \\ & 0 & e^{i\varphi_{23}} & 0 & \gamma e^{i\varphi_{25}} & \gamma e^{i\varphi_{14}} \\ & & 0 & \gamma e^{i\varphi_{25}} & 0 & \gamma e^{i\varphi_{15}} \\ & & & 0 & e^{-i\varphi_{23}} & e^{i\varphi_{12}} \\ & & & & 0 & e^{i\varphi_{13}} \\ & & & & & 0 \end{pmatrix} \quad (\text{S1})$$

with $t_1 = \gamma t$,

$$\varphi_{12} = -a \sin\left(\frac{\pi}{6} - \theta\right) k_x - a \cos\left(\frac{\pi}{6} - \theta\right) k_y,$$

$$\varphi_{13} = a \sin\left(\frac{\pi}{6} + \theta\right) k_x - a \cos\left(\frac{\pi}{6} + \theta\right) k_y,$$

$$\varphi_{14} = \left[-\frac{a}{2} - \frac{\sqrt{3}b}{2} + \frac{\sqrt{3}}{3} a \cos\left(\frac{\pi}{6} + \theta\right) + \frac{\sqrt{3}}{3} a \sin\theta \right] k_x + \left[\frac{\sqrt{3}a}{6} + \frac{b}{2} + \frac{\sqrt{3}}{3} a \sin\left(\frac{\pi}{6} + \theta\right) - \frac{\sqrt{3}}{3} a \cos\theta \right] k_y,$$

$$\varphi_{15} = \left[\frac{a}{2} + \frac{\sqrt{3}b}{2} - \frac{\sqrt{3}}{3} a \cos\left(\frac{\pi}{6} - \theta\right) + \frac{\sqrt{3}}{3} a \sin\theta \right] k_x + \left[\frac{\sqrt{3}a}{6} + \frac{b}{2} + \frac{\sqrt{3}}{3} a \sin\left(\frac{\pi}{6} - \theta\right) - \frac{\sqrt{3}}{3} a \cos\theta \right] k_y,$$

$$\varphi_{23} = a\cos\theta k_x + a\sin\theta k_y,$$

$$\begin{aligned} \varphi_{25} = & -\frac{\sqrt{3}}{3} \left[a\sin\left(\frac{\pi}{3} + \theta\right) - a\sin\left(\frac{\pi}{3} - \theta\right) \right] k_x \\ & + \left[\frac{\sqrt{3}}{3} a\cos\left(\frac{\pi}{3} - \theta\right) + \frac{\sqrt{3}}{3} a\cos\left(\frac{\pi}{3} + \theta\right) - \frac{\sqrt{3}}{3} a - b \right] k_y. \end{aligned}$$

Hereafter, a and b represent the side length of the regular triangle and distance between adjacent regular triangles of the perfect Ruby lattice, as shown in Fig. 2(a) of the main text. Only half of the matrix for simplification is presented in the Hamiltonian matrix. The whole matrix is filled to ensure a Hermitian matrix.

m -Ruby lattice

$$H_0^{mR}(\mathbf{k}) = -t \begin{pmatrix} 0 & e^{i\varphi_{12}} & e^{i\varphi_{13}} & \mu e^{i\varphi_{14}} & v e^{i\varphi_{15}} & 0 \\ & 0 & e^{i\varphi_{23}} & 0 & \mu e^{i\varphi_{25}} & v e^{i\varphi_{26}} \\ & & 0 & v e^{i\varphi_{34}} & 0 & \mu e^{i\varphi_{36}} \\ & & & 0 & e^{i\varphi_{45}} & e^{i\varphi_{46}} \\ & & & & 0 & e^{i\varphi_{56}} \\ & & & & & 0 \end{pmatrix} \quad (\text{S2})$$

with $t_1 = \mu t$, $t_1' = vt$,

$$\varphi_{12} = -a\sin\left(\frac{\pi}{6} - \theta\right) k_x - a\cos\left(\frac{\pi}{6} - \theta\right) k_y,$$

$$\varphi_{13} = a\sin\left(\frac{\pi}{6} + \theta\right) k_x - a\cos\left(\frac{\pi}{6} + \theta\right) k_y,$$

$$\begin{aligned} \varphi_{14} = & \left[-\frac{a}{2} - \frac{\sqrt{3}b}{2} + \frac{\sqrt{3}}{3} a\cos\left(\frac{\pi}{6} - \theta\right) + \frac{\sqrt{3}}{3} a\sin\theta \right] k_x \\ & + \left[\frac{\sqrt{3}a}{6} + \frac{b}{2} + \frac{\sqrt{3}}{3} a\sin\left(\frac{\pi}{6} - \theta\right) - \frac{\sqrt{3}}{3} a\cos\theta \right] k_y, \end{aligned}$$

$$\begin{aligned} \varphi_{15} = & \left[\frac{a}{2} + \frac{\sqrt{3}b}{2} - \frac{\sqrt{3}}{3} a\cos\left(\frac{\pi}{6} + \theta\right) + \frac{\sqrt{3}}{3} a\sin\theta \right] k_x \\ & + \left[\frac{\sqrt{3}a}{6} + \frac{b}{2} + \frac{\sqrt{3}}{3} a\sin\left(\frac{\pi}{6} + \theta\right) - \frac{\sqrt{3}}{3} a\cos\theta \right] k_y, \end{aligned}$$

$$\varphi_{23} = a\cos\theta k_x + a\sin\theta k_y,$$

$$\varphi_{25} = \left[\frac{2\sqrt{3}}{3} a \cos\left(\frac{\pi}{3} - \theta\right) - \frac{\sqrt{3}}{3} a - b \right] k_y,$$

$$\begin{aligned} \varphi_{26} = & \left[-\frac{a}{2} - \frac{\sqrt{3}b}{2} + \frac{\sqrt{3}}{3} a \cos\left(\frac{\pi}{6} + \theta\right) - \frac{\sqrt{3}}{3} a \sin\theta \right] k_x \\ & + \left[\frac{\sqrt{3}a}{6} + \frac{b}{2} + \frac{\sqrt{3}}{3} a \sin\left(\frac{\pi}{6} + \theta\right) - \frac{\sqrt{3}}{3} a \cos\theta \right] k_y, \end{aligned}$$

$$\varphi_{34} = \left[\frac{2\sqrt{3}}{3} a \cos\left(\frac{\pi}{3} + \theta\right) - \frac{\sqrt{3}}{3} a - b \right] k_y,$$

$$\begin{aligned} \varphi_{36} = & \left[\frac{a}{2} + \frac{\sqrt{3}b}{2} - \frac{\sqrt{3}}{3} a \cos\left(\frac{\pi}{6} - \theta\right) - \frac{\sqrt{3}}{3} a \sin\theta \right] k_x \\ & + \left[\frac{\sqrt{3}a}{6} + \frac{b}{2} + \frac{\sqrt{3}}{3} a \sin\left(\frac{\pi}{6} - \theta\right) - \frac{\sqrt{3}}{3} a \cos\theta \right] k_y, \end{aligned}$$

$$\varphi_{45} = -a \cos\theta k_x + a \sin\theta k_y,$$

$$\varphi_{46} = -a \sin\left(\frac{\pi}{6} + \theta\right) k_x - a \cos\left(\frac{\pi}{6} + \theta\right) k_y,$$

$$\varphi_{56} = a \sin\left(\frac{\pi}{6} - \theta\right) k_x - a \cos\left(\frac{\pi}{6} - \theta\right) k_y.$$

***a*-Ruby lattice**

$$H_0^{aR}(\mathbf{k}) = -t \begin{pmatrix} 0 & e^{i\varphi_{12}} & e^{i\varphi_{13}} & \mu e^{i\varphi_{14}} & v e^{i\varphi_{15}} & \xi e^{i\varphi_{16}} \\ & 0 & e^{i\varphi_{23}} & \xi e^{i\varphi_{24}} & \mu e^{i\varphi_{25}} & v e^{i\varphi_{26}} \\ & & 0 & v e^{i\varphi_{34}} & \xi e^{i\varphi_{35}} & \mu e^{i\varphi_{36}} \\ & & & 0 & e^{i\varphi_{45}} & e^{i\varphi_{46}} \\ & & & & 0 & e^{i\varphi_{56}} \\ & & & & & 0 \end{pmatrix} \quad (\text{S3})$$

with $t_1 = \mu t$, $t'_1 = v t$, $t_2 = \xi t$,

$$\varphi_{12} = -a \sin\left(\frac{\pi}{6} - \theta\right) k_x - a \cos\left(\frac{\pi}{6} - \theta\right) k_y,$$

$$\varphi_{13} = a \sin\left(\frac{\pi}{6} + \theta\right) k_x - a \cos\left(\frac{\pi}{6} + \theta\right) k_y,$$

$$\varphi_{14} = \left(-\frac{\sqrt{3}b}{2} + \frac{\sqrt{3}}{3} a \sin\theta \right) k_x + \left(\frac{\sqrt{3}a}{3} + \frac{b}{2} - \frac{\sqrt{3}}{3} a \cos\theta \right) k_y,$$

$$\varphi_{15} = \left(\frac{\sqrt{3}b}{2} + \frac{\sqrt{3}}{3} \text{asin}\theta \right) k_x + \left(\frac{\sqrt{3}a}{3} + \frac{b}{2} - \frac{\sqrt{3}}{3} \text{acos}\theta \right) k_y,$$

$$\varphi_{16} = \left(-\frac{a}{2} - \frac{\sqrt{3}b}{2} + \frac{\sqrt{3}}{3} \text{asin}\theta \right) k_x + \left(-\frac{\sqrt{3}a}{6} + \frac{b}{2} - \frac{\sqrt{3}}{3} \text{acos}\theta \right) k_y,$$

$$\varphi_{23} = \text{acos}\theta k_x + \text{asin}\theta k_y,$$

$$\varphi_{24} = \left[\frac{a}{2} + \frac{\sqrt{3}}{3} \text{asin}\left(\frac{\pi}{3} - \theta\right) \right] k_x + \left[-\frac{\sqrt{3}a}{6} - b + \frac{\sqrt{3}}{3} \text{acos}\left(\frac{\pi}{3} - \theta\right) \right] k_y,$$

$$\varphi_{25} = \left[-\frac{a}{2} + \frac{\sqrt{3}}{3} \text{asin}\left(\frac{\pi}{3} - \theta\right) \right] k_x + \left[-\frac{\sqrt{3}a}{6} - b + \frac{\sqrt{3}}{3} \text{acos}\left(\frac{\pi}{3} - \theta\right) \right] k_y,$$

$$\varphi_{26} = \left[-\frac{a}{2} - \frac{\sqrt{3}b}{2} + \frac{\sqrt{3}}{3} \text{asin}\left(\frac{\pi}{3} - \theta\right) \right] k_x + \left[-\frac{\sqrt{3}a}{6} + \frac{b}{2} + \frac{\sqrt{3}}{3} \text{acos}\left(\frac{\pi}{3} - \theta\right) \right] k_y,$$

$$\varphi_{34} = \left[\frac{a}{2} - \frac{\sqrt{3}}{3} \text{asin}\left(\frac{\pi}{3} + \theta\right) \right] k_x + \left[-\frac{\sqrt{3}a}{6} - b + \frac{\sqrt{3}}{3} \text{acos}\left(\frac{\pi}{3} + \theta\right) \right] k_y,$$

$$\varphi_{35} = \left[\frac{\sqrt{3}b}{2} - \frac{\sqrt{3}}{3} \text{asin}\left(\frac{\pi}{3} + \theta\right) \right] k_x + \left[\frac{\sqrt{3}a}{3} + \frac{b}{2} + \frac{\sqrt{3}}{3} \text{acos}\left(\frac{\pi}{3} + \theta\right) \right] k_y,$$

$$\varphi_{36} = \left[\frac{a}{2} + \frac{\sqrt{3}b}{2} - \frac{\sqrt{3}}{3} \text{asin}\left(\frac{\pi}{3} + \theta\right) \right] k_x + \left[-\frac{\sqrt{3}a}{6} + \frac{b}{2} + \frac{\sqrt{3}}{3} \text{acos}\left(\frac{\pi}{3} + \theta\right) \right] k_y,$$

$$\varphi_{45} = -ak_x,$$

$$\varphi_{46} = -\frac{a}{2}k_x - \frac{\sqrt{3}a}{2}k_y,$$

$$\varphi_{56} = \frac{a}{2}k_x - \frac{\sqrt{3}a}{2}k_y.$$

***b*-Ruby lattice**

$$H_0^{bR}(\mathbf{k}) = -t \begin{pmatrix} 0 & ve^{i\varphi_{12}} & ve^{i\varphi_{13}} & \mu e^{i\varphi_{14}} & \mu e^{i\varphi_{15}} & 0 \\ & 0 & ve^{i\varphi_{23}} & 0 & \mu e^{i\varphi_{25}} & \mu e^{i\varphi_{26}} \\ & & 0 & \mu e^{i\varphi_{34}} & 0 & \mu e^{i\varphi_{36}} \\ & & & 0 & e^{i\varphi_{45}} & e^{i\varphi_{46}} \\ & & & & 0 & e^{i\varphi_{56}} \\ & & & & & 0 \end{pmatrix} \quad (\text{S4})$$

with $t_1 = \mu t$, $t' = vt$,

$$\begin{aligned}
\varphi_{12} &= -\frac{a'}{2}k_x - \frac{\sqrt{3}a'}{2}k_y, \\
\varphi_{13} &= \frac{a'}{2}k_x - \frac{\sqrt{3}a'}{2}k_y, \\
\varphi_{14} &= -\frac{\sqrt{3}b}{2}k_x + \left(\frac{\sqrt{3}a}{3} + \frac{b}{2} - \frac{\sqrt{3}}{3}a'\right)k_y, \\
\varphi_{15} &= \frac{\sqrt{3}b}{2}k_x + \left(\frac{\sqrt{3}a}{3} + \frac{b}{2} - \frac{\sqrt{3}}{3}a'\right)k_y, \\
\varphi_{23} &= a'k_x \\
\varphi_{25} &= \frac{1}{2}(a' - a)k_x + \left(\frac{\sqrt{3}}{6}a' - \frac{\sqrt{3}}{6}a - b\right)k_y, \\
\varphi_{26} &= \left(-\frac{a}{2} - \frac{\sqrt{3}b}{2} + \frac{a'}{2}\right)k_x + \left(-\frac{\sqrt{3}a}{6} + \frac{b}{2} + \frac{\sqrt{3}}{6}a'\right)k_y, \\
\varphi_{34} &= \frac{1}{2}(a - a')k_x + \left(\frac{\sqrt{3}}{6}a' - \frac{\sqrt{3}}{6}a - b\right)k_y, \\
\varphi_{36} &= \left(\frac{a}{2} + \frac{\sqrt{3}b}{2} - \frac{a'}{2}\right)k_x + \left(-\frac{\sqrt{3}a}{6} + \frac{b}{2} + \frac{\sqrt{3}}{6}a'\right)k_y, \\
\varphi_{45} &= -ak_x, \\
\varphi_{46} &= -\frac{a}{2}k_x - \frac{\sqrt{3}a}{2}k_y, \\
\varphi_{56} &= \frac{a}{2}k_x - \frac{\sqrt{3}a}{2}k_y.
\end{aligned}$$

III. Spin-Orbit Coupling (SOC) of *i*-Ruby Lattice

In the main text, only one spin channel was considered. So spin-splitting scenario was not displaced. Here, we considered the SOC of the two spin channels in the electronic band structure calculations of the *i*-Ruby lattice and the nanoribbons, as shown in Fig. S1. Clearly, the degeneracy of the two spins is lifted in the electronic band structures of *i*-Ruby lattice, as shown in Fig.S1(a). For the *i*-Ruby nanoribbon, two topological edge bands emerge within the band gap due to the SOC, demonstrating the QSHE characteristics, as shown in Fig. S1(b). The topological

features revealed in the one-spin strategy are well-reproduced in the two-spin strategy.

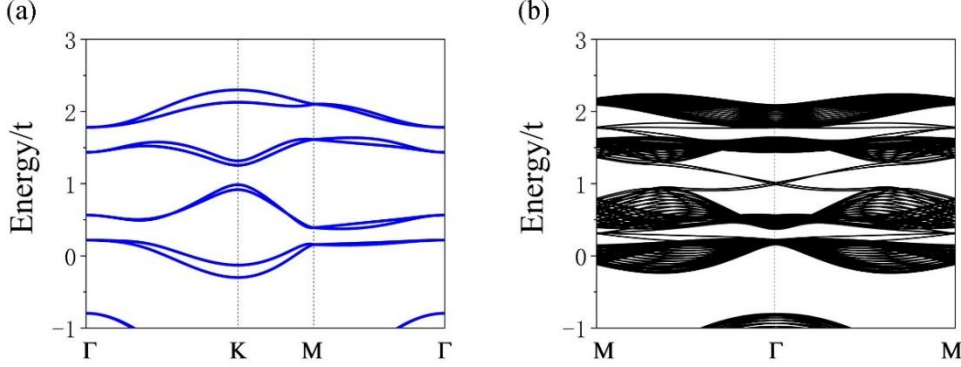


Fig. S1 The electronic bands structures of (a) *i*-Ruby lattice and (b) the nanoribbons with SOC.

SIII. Effects of Hopping Amplitude on Energy Bands

We calculated the electronic band structures of *i*-Ruby lattice with different t_1/t_0 ratios ranging from 0 to 2.0 to uncover the possible quantum phase transition, as shown in Fig. S2. For $t_1/t_0 = 0$, all the bands become dispersionless, because the hopping between triangles disappears, leading to highly-localize electronic states. With the increase of t_1/t_0 , the bands become more dispersive. The Fermi velocity (v_F) of the Dirac bands increases with the increases of t_1/t_0 , as shown in Fig. S2(d). Moreover, the t_1/t_0 ratio affects the band degeneracy. We defined two band gaps, ΔE_1 and ΔE_2 to describe the variation of the band degeneracy. From Fig. S2, we can see that $\Delta E_1 > 0; \Delta E_2 = 0$ as $t_1/t_0 < 1$ and $\Delta E_1 = 0; \Delta E_2 > 0$ as $t_1/t_0 > 1$. At the critical point of $t_1/t_0 = 1$, $\Delta E_1 = \Delta E_2 = 0$, leads to a three-fold (six-fold considering spins) flat band along the Γ -M direction, as shown in Fig. S2(b).

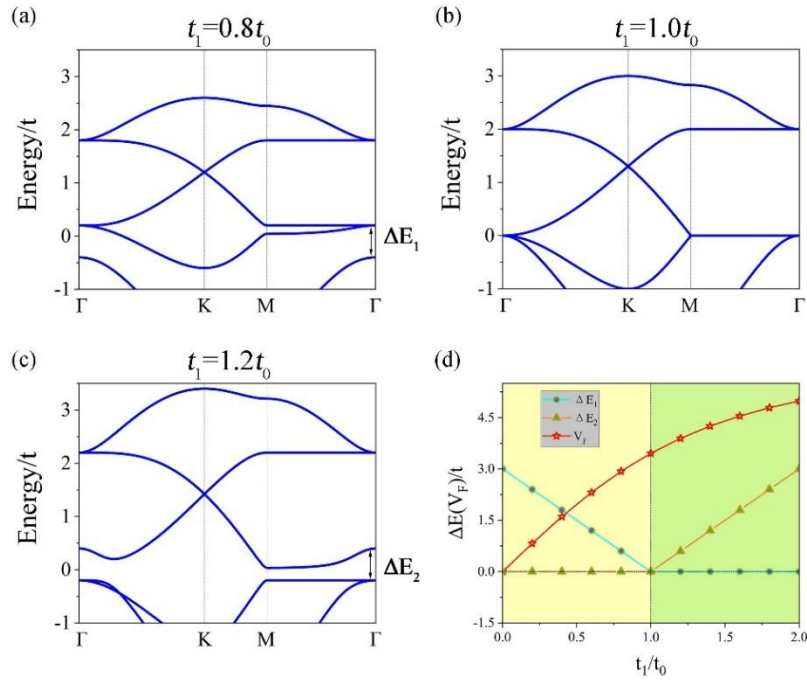


Fig. S2 The electronic band structures of *i*-Ruby lattice with (a) $t_1/t_0=0.8$; (b) $t_1/t_0=1.0$; (c) $t_1/t_0 = 1.2$. (d) The variation of Fermi velocity, ΔE_1 and ΔE_2 as a function of t_1/t_0 .